UNIVERSITY OF CALIFORNIA
SANTA CRUZ

METHODS FOR IMPROVING THE PERFORMANCE OF STRUCTURED ILLUMINATION MICROSCOPY WITH ADAPTIVE OPTICS

A thesis submitted in partial satisfaction of the
requirements for the degree of

MASTER OF SCIENCE

in

ELECTRICAL ENGINEERING

by

Alex Bardales

December 2018

The Thesis of Alex Bardales
is approved:

Marco Rolandi, Chair

Sara Abrahamsson

Farid Dowla

Lori Kletzer
Vice Provost and Dean of Graduate Studies

Table of Contents

List of Figures

List of Tables

Abstract

Methods for Improving the Performance of Structured Illumination Microscopy with Adaptive Optics

by

Alex Bardales

While the light microscope offers biologists the advantage *in vivo* imaging, it suffers from a reduced resolution due to constraints imposed in the optical domain. The hard limit on resolving power, known as the diffraction limit of resolution, is the distance of roughly one-half wavelength of the excitation light of an imaging system. Super-resolution imaging can relax the constraint on resolution.

Further constraints on resolving power are imposed by light wavefront aberrations. Sample-induced aberrations are inherent to biological samples. Other aberrations come from the microscope system itself. The canonical solution for wavefront aberration in a microscope is known as adaptive optics (AO).

Structured Illumination Microscopy (SIM) is an optical transfer function-based super-resolution technique that increases the support region in Fourier space via spatial frequency mixing. In particular, the optical imaging system that acts as a low-pass filter on the image of the biological sample, favors low spatial frequencies. By optically mixing the biological sample with SIM fringes, high spatial frequency information from the sample is mixed into the pass band of the microscope.

This work contains the results of a SIM microscope implementation with an adaptive optics system (AOSIM). The results of this microscope are presented. In addition, further improvements for AO SIM microscopes are given, backed by simulations based on the mathematics of SIM and both Fourier and geometric optics. The simulations show the utility of the improvements in terms of both aberration mitigation and resolution improvement.

Dedicated to my family and to my advisor Joel Kubby.

Acknowledgments

The results presented herein were obtained at the W.M. Keck Center for Adaptive Optical Microscopy (CfAOM) at University of California Santa Cruz. The CfAOM was made possible by the generous financial support of the W.M. Keck Foundation. This material is also based upon work supported by the National Science Foundation under Grant. Numbers 1353461 & 1429810. Any opinions, findings, and conclusions or recommendations expressed in this material are those of the authors and do not necessarily reflect the views of the National Science Foundation.

Chapter 1

Introduction

Many important features in biological microscopy are on the order of 10's to 100's of nanometers [28]. To view these features, biologists have at their disposal several classes of microscopes. The type of microscope that is most suitable for *in vivo* imaging is the light microscope. The light microscope thus plays an important role in bio-imaging [26, 44], due to its relatively non-invasive operation. With a light microscope, biologists can capture images of live samples.

Microscopy systems that use visible light are not without their problems. The two main disadvantages of the light microscope for biology are (1) its resolving power, and (2) sample-induced aberrations. The limit on resolving power is due to the wave nature of light, which fundamentally limits a microscope's resolution to approximately half the wavelength of excitation light [10]. The source of aberrations are inherent to the both the biological sample and the optical imaging system. This thesis will cover topics that address these problems that are associated with light microscopy, in the hope that the contributions will advance the state of the art of *in vivo* biological microscopy.

1.1 Super resolution imaging

In the past decade, many methods that have reached a spatial resolution beyond the diffraction limit have been reported in the literature [6, 21, 25]. These methods are collectively referred to as super-resolution (SR) microscopy. For example, the invention of stimulated emission depletion microscopy [25], photoactivated localization microscopy [6], and structured illumination microscopy [20, 22, 23] have all given scientists the ability to image features beyond the diffraction limit of light.

1.2 Structured illumination microscopy

Structured illumination microscopy (SIM) refers to a super-resolution microscope and its accompanying image reconstruction algorithm [20]. Linear SIM gives a modest super-resolution factor of 2x [48], but is less invasive and faster than the other SR techniques. SIM works by projecting illumination patterns onto the sample and acquiring raw "SIM" images. The SIM reconstruction algorithm then extracts high-resolution information from aliased raw data in Fourier space such that high spatial frequency information is aliased into the pass-band of the microscope. A convenient illumination pattern is sinusoidal, because this has a simple Fourier domain representation.

SIM is referred to as an optical transfer function (OTF)-based super-resolution technique. That is, SIM works to increase the OTF support region in Fourier space via spatial frequency mixing. In particular, the optical imaging system acts as a low-pass filter on the image of the biological sample, which constrains the OTF to low spatial frequencies. By optically mixing the biological sample with SIM fringes, high spatial frequency information from the sample is mixed down into

the pass band of the microscope.

In addition to super-resolution, SIM techniques can also be applied to 3D imaging systems as a method of optical sectioning. This technique, known as "sectioning SIM", is a method for rejecting out-of-focus light that comes from axial regions above and below the focal plane within the sample. In either case, SIM requires that a high-contrast, high-fidelity SIM pattern be projected into the biological sample. Typically, SIM patterns are generated in the sample via two-beam interference, which is obtained by projecting the ± 1 diffractive orders of light from a diffractive grating onto the back aperture of the microscope objective.

1.3 Adaptive optics

To address the issue of light aberrations, adaptive optics (AO) has been introduced into microscopy. AO has been successful in removing some aberrations induced by the sample and the optical system. Most AO systems place the corrective element at a plane conjugate to the pupil plane of the microscope. Recalling the fact that the pupil plane is the Fourier dual of the focal plane in the sample, we note that the Fourier transform of the SIM fringes are impulse-like functions at the pupil plane. Therefore, it is not possible to make AO corrections on the SIM fringes in the excitation path of the microscope, since the two diffractive orders are too small to be affected by wavefront correction.

Chapter 2

SIM Framework

2.1 Introduction

We begin this chapter with the framework for SIM, which follows, roughly, the work done in [20, 50, 23]. In this discussion, we will refer to three different images. The first is the image that which we would like to see, but are not able to, because of the low-pass filtering action of microscope objective lens. We will refer to this image as the ground truth, the sample under observation which contains unobservable, high frequency information. The image that we can observe with the microscope is called just that: the observable image. The third image is called the illumination pattern. This is the structured pattern that will be used to heterodyne the high frequency information into the pass band of the optical system.

Structured illumination microscopy is inherently tied to Fourier optics. Fourier analysis speaks to the duality of real and reciprocal spaces of an image. In the setting of an analog optical system, one such duality is the relation between the point spread function (PSF) and the optical transfer function (OTF) of the microscope.

The PSF exists in real space and represents the impulse response function of

the system. In optics, an "impulse" is a point source of light, so the PSF represents the smallest point source which can observed under the effect the optical system (i.e. the microscope). In a diffraction-limited optical system, the PSF can actually be measured by attempting to observe a fluorescent nanobead, for example, whose size is on the order of magnitude of half a wavelength of the fluorescent spectrum. In Chapter 3, we use a 0.11μm nanobead for this purpose.

Given knowledge of the PSF of an optical system, we can understand the spatial limit of resolution in terms of the convolution of the ground truth and the PSF. In digital image processing, the PSF represented as the blur kernel of the system.

The OTF is the Fourier dual of the PSF in a coherent light imaging system. This function belongs to the class of $C_0(\mathbf{R})$ functions, or those functions which vanish at infinity, but the magnitude becomes very close to zero at and beyond the cutoff frequency of the system. Thus the imaging system acts as a low-pass filter on the ground truth. Any high frequency information becomes nulled (filtered out) by the optical system itself.

In real space, high frequency information corresponds to components that are very close together. To illustrate with a simple example, consider a pair of two point-like sources that are far enough apart that each point is individually resolvable. However, as these two point sources get closer, the observable image of the two points under the effect of the OTF begins to show two points as if they were merged into one. The minimum distance between the two points at which they are individually resolvable is known as the resolution limit of the microscope. In a diffraction-limited system, this distance becomes equivalent to the diffraction limit of light itself, which is known as the Rayleigh criterion[45]. For a microscope, this distance is approximately $\frac{\lambda}{2NA}$.

Viewed from the perspective of the Fourier domain, the goal of super-resolution imaging is to increase the cutoff frequency of the OTF of a microscope so that it extends the observable region beyond frequencies that are diffraction-limited due to the wave nature of light. The SIM method for increasing the OTF support is discussed in the next section.

2.2 The Mathematics of SIM

For any point $\mathbf{r}$ in real space, we denote the ground truth by $D(\mathbf{r})$ and the observable image by $D'(\mathbf{r})$. These functions are related to the OTF, $H(\mathbf{r})$ by the following (for brevity we have combined this equation with its Fourier dual):

$$D'(\mathbf{r}) = D(\mathbf{r}) \otimes H(\mathbf{r}) \Longleftrightarrow D'(\mathbf{k}) = D(\mathbf{k}) \cdot H(\mathbf{k}), \tag{2.1}$$

where $\otimes$ denotes the convolution operator, and $\mathbf{k}$ being a point in reciprocal space.

Next, we address the illumination pattern, $I(\mathbf{r})$. If we make this illumination pattern a sinusoid, then its illumination intensity can be given by

$$I(\mathbf{r}) = \frac{1}{2}[1 + \cos(2\pi \mathbf{p}_k \cdot \mathbf{r} + \phi_n)], \tag{2.2}$$

where $\mathbf{p}$ is the spatial frequency vector of the illumination pattern, and ϕ_n is a phase shift. For conventional SIM reconstructions, n ranges from 1 to 3, while the k evenly divides the unit circle in 3 parts. With all possible combinations of $\mathbf{p}_k$ and ϕ_n, we have that there will be nine images per SIM reconstruction.

Another convenience of this illumination pattern is seen in its spatial-frequency domain representation which is a sum of three of delta functions:

$$I(\mathbf{k}) = \frac{1}{2}\left[\delta(\mathbf{k}) + \frac{1}{2}\delta(\mathbf{k} - \mathbf{p}_k)e^{-j\phi} + \frac{1}{2}\delta(\mathbf{k} + \mathbf{p}_k)e^{+j\phi}\right], \tag{2.3}$$

and if we mix (or multiply) Equation 2.2 with the ground truth image, then we obtain

$$D'(\mathbf{r}) = D(\mathbf{r})I(\mathbf{r}) \otimes H(\mathbf{r}) \Longleftrightarrow D'(\mathbf{k}) = [D(\mathbf{k}) \otimes I(\mathbf{k})]H(\mathbf{k}). \tag{2.4}$$

The convolution theorem allows us to write the spectrum of $D'(\mathbf{k})$ as

$$D'(\mathbf{k}) = \frac{1}{2}\left[D(\mathbf{k}) + \frac{1}{2}D(\mathbf{k}-\mathbf{p}_k)e^{-j\phi} + \frac{1}{2}D(\mathbf{k}+\mathbf{p}_k)e^{+j\phi}\right] \cdot H(\mathbf{k}), \tag{2.5}$$

so we see that under the illumination pattern $I(\mathbf{r})$, the spectrum of the observable image is a linear, phase-shifted combination of the ground truth. Here we note that lower spatial frequencies of $D(\mathbf{k})$ already fall within the pass band of the OTF, $H(\mathbf{k})$, but $D(\mathbf{k} \pm \mathbf{p}_k)$ do not lie within the pass band.

If we use different phases, then we can have a series of measurements that can be represented in matrix form as

$$\begin{bmatrix} D'_1(\mathbf{k}) \\ D'_2(\mathbf{k}) \\ \vdots \\ D'_N(\mathbf{k}) \end{bmatrix} = \begin{bmatrix} 1 & e^{j\phi_1} & e^{-j\phi_1} \\ 1 & e^{j\phi_2} & e^{-j\phi_2} \\ \vdots & \vdots & \vdots \\ 1 & e^{j\phi_N} & e^{-j\phi_N} \end{bmatrix} \times \begin{bmatrix} \frac{1}{2}H(\mathbf{k})D(\mathbf{k}) \\ \\ \frac{1}{4}H(\mathbf{k})D(\mathbf{k}-\mathbf{p}_k) \\ \\ \frac{1}{4}H(\mathbf{k})D(\mathbf{k}+\mathbf{p}_k) \end{bmatrix}. \tag{2.6}$$

However, in this work we will use only three phases, 0, $2\pi/3$, and $4\pi/3$, as this is the minimum number of known variables needed to solve for three unknown equations.

It is the second two rows of the rightmost matrix in Equation 2.6, the terms with $1/4H(\mathbf{k})D(\mathbf{k}\pm\mathbf{p}_k)$, that contain the super-resolution information. By heterodyning these frequencies into the passband of the microscope, the SR information

can be recovered. In the reconstruction step, we move these SR spatial frequency components, $D(\mathbf{k} \pm \mathbf{p}_k)$, back to their original location in reciprocal space. Since this shift operation involves overlapping regions, there may be more than one estimate for a given point in reciprocal space. A weighted average can be implemented to obtain an overall Fourier representation of the SR image. A Wiener filter is also typically used to suppress numerical instability, and artifacts may appear.

This mathematical framework demonstrates how SIM effectively increases the pass-band of the OTF. After recovering the enlarged Fourier domain representation of the object, we perform an inverse Fourier transform. In this way, we can recover the high-spatial frequency information that was originally outside the pass-band of the microscope OTF.

Chapter 3

Implemention of an AOSIM Microscope

3.1 Introduction

A light microscope is preferred for biological imaging of *in vivo* samples because of its non-invasive properties. However, the light microscope is not without its limitations. The two primary limitations, noted in Chapter 1, are the resolution limit and sample-induced aberrations. This chapter describes our super-resolution SIM microscope with AO correction for both high and low order aberrations.

Our work at the CfAOM in this area began 2014, in which we posited a dual AO corrective system. In [30] we use the term "woofer-tweeter" as a heuristic to describe the system of dual AO corrective elements. Our work extended that of [11], in which the authors developed a scanning laser ophthalmoscope (SLO). The name "woofer" is borrowed from the acoustic speaker that operates on low-frequency sound. In our context, the "woofer" describes the deformable mirror (DM) that corrects the high-magnitude, low order wavefront aberrations. On the

other hand, the purpose of the "tweeter" DM is to correct for the low-amplitude, high-frequency wavefront aberrations[1].

3.2 Adaptive optics

In order to redirect the light into the small focal area where it supposed to be, adaptive optics [31] is vitally important. One way is direct measurement of the aberrated wavefront using a wavefront sensor with a feedback loop to a deformable mirror (DM) which iteratively reduces an error term. The wavefront can be measured by either introducing an artificial guide star [3, 4, 59] or using a sample that has been labeled with fluorescent proteins [55, 54, 2]. Recently, Tao, et al. [56], reported the measurement of the wavefront from auto-fluorescent light from within the sample.

In direct wavefront measurement mode, the AO correction can be done using either open or closed-loop control. In the first method, the wavefront is continuously measured and fed back to the DM until the corrected wavefront error is below a specified threshold. This approach requires a calibrated DM system and is able to make the correction faster since it is done in a single step without iterations. The closed-loop method, on the other hand, is better able to eliminate wavefront error, but is more time-consuming because of the feedback control loop.

[1]The analogy breaks down when considering the action of the woofer-tweeter heuristic: In the wavefront aberration setting, the woofer (tweeter) DM is used to mitigate low (resp. high) frequency phenomena, while the in the acoustic setting, the speakers are used to produce and amplify sound waves.

3.3 SIM fringes

In a SIM microscope, the term "SIM fringes," or "illumination pattern," refers to the spatial sinusoid that is projected onto the sample in the image plane. The fringes are the result of the two beam interference phenomena that will be described below. This spatial sinusoid is the light intensity function that is described by Equation 2.2 and satisfies the SIM matrix equation (Equation 2.6). In other words, two-beam interference is optical effect that produces spatial frequency heterodyning possible, and thus makes super-resolution possible within the SIM framework.

The SIM fringes are projected onto the image plane as a result of the interference of two coherent light beams. The original SIM microscopes would produce this effect by shining light onto a diffractive grating and then blocking out all but the ± 1 diffraction orders[2]. In our microscope, we use a digital light projector (DLP) – also known as a digital micromirror device (DMD) – rather than a diffractive grating. This device is a matrix of micro mirrors that can be switched into the "on" or "off" state, and by applying the appropriate function to the mirrors, we can simulate the effect of the diffractive grating (Figure 3.1). The benefit of using the DMD is that there is no need to mechanically rotate the diffractive grating to acquire images that satisfy the three different orientations (the $\mathbf{p}_k$ vector from Equation 2.2). The DMD has a refresh frequency in the range of kilo-Hertz, which is much faster than a mechanically rotating grating. The phase shifts (ϕ_k from Equation 2.2 are likewise updated very fast on a DMD, in contrast with a grating that must undergo mechanical translation in a lateral direction.

In the SIM reconstruction method, images are taken at with the SIM fringes rotated at different angles, and different phase shifts in the patterned excitation

[2]Non-linear SIM is typically done by letting higher diffraction orders pass through to the sample.

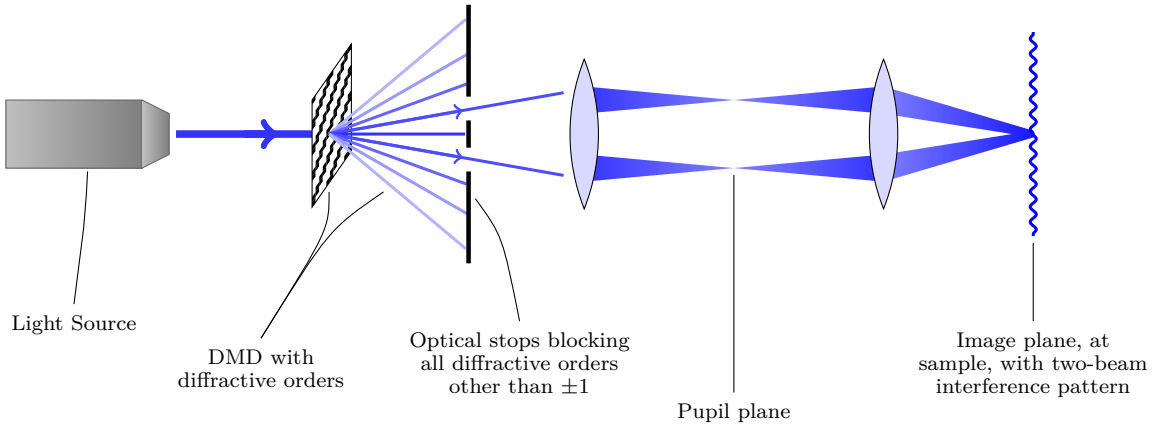

Figure 3.1: Diagram of the excitation light path. The excitation light in our microscope comes from a 488nm laser light source, which is in the blue region of visible light.

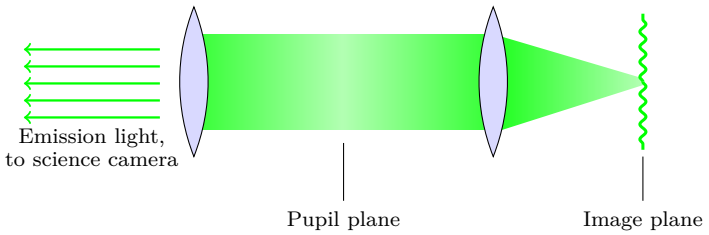

Figure 3.2: Diagram of the emission light path. The emission light that leaves the sample has a slightly longer wavelength than the excitation wavelength, due to the Stokes shift. The emission light is due to green flourescent protein labels (GFP) in the sample, which has a wavelength of 511nm.

[20, 50]. In 2D SIM, typically nine images are required (3 phase shifts per each of three rotations of the SIM fringes). This number is consistent with Equation 2.6.

3.4 Previous Work

The benefits of adaptive optics applied to several types of light microscopy have been reported. Examples include AO confocal microscopy [31, 9], AO two-photon microscopy [13, 56], and AO structured illumination microscopy [57, 41]. AO correction provides better resolution, signal-to-noise ratio, contrast, and enables deeper penetration depth. Recently, Thomas et al. [57] reported on the application of AO to structured illumination microscopy. In their wavefront sensorless system, a deformable mirror, the Mirao 52-e from Imagine Optics, was employed to compensate the wavefront aberration. Imaging a fluorescent nanoparticle under a 35 μm thick C. elegans worm an 140 nm FWHM of the PSF was reported in their results after AO correction. While it decreased the width of the PSF, super resolution imaging was not demonstrated since two features below the diffraction limit were not resolved. Although a high Strehl ratio of 0.8 was obtained after AO correction of the aberration caused from the C. elegans, a drawback of this system is that it is not able to correct high-spatial frequency aberrations since the DM that was used (Mirao 52-e) has only 52 actuators (only 36 of the actuators are in the 15 mm effective aperture). The sensorless mode for wavefront correction also may not be suitable for a sample with dynamic aberrations.

To overcome the previously discussed light microscopy limitations, Diana Chen et al. introduced a dual-deformable mirror adaptive optical system into a confocal microscope to enable high-order, high-amplitude wavefront correction and showed improvements in the dynamic range and quality of the wavefront correction for images of the human retina [11].

3.5 Woofer-Tweeter AO SIM Microscope

In this section, we introduce the dual AO system into a widefield structured illumination microscope. The benefits from the dual-deformable mirror (DM) configuration are the ability to compensate both large-amplitude and high-spatial frequency wavefront aberrations to enable SIM in thick specimens. After correcting the wavefront aberration, the near-diffraction limited PSF is further enhanced by using the structured illumination method.

As illustrated in Figure 3.3, the dual-DM, woofer and tweeter components are placed in planes conjugated to the back pupil of the objective lens. The "tweeter" is a MEMS deformable mirror from Boston Micromachines that has 140 actuators with a maximum stroke of 3.5 μm. It is set to correct low-amplitude, high-spatial frequency wavefront errors. The "woofer" is a membrane deformable mirror (Mirao 52-e) from Imagine Optics with 52 actuators and a maximum stroke of $\pm$ 50 μm. It is designed to correct the low-spatial frequency but high-amplitude wavefront errors.

In order to be suitable for live imaging, we utilize a fast direct wavefront measurement system known as the Shack-Hartmann wavefront sensor (SHWS) [42] that includes a 44×44 lenslet array, of which 97 are in the active aperture. Each lenslet of the SHWS has a focal length of 24 mm and is placed on a pitch of 0.328 mm to form the array.

Images are captured with an Andor science camera. The science camera is an EMCCD camera (Andor iXon), with 1004×1002 pixels. The microscope objective is a 60× water-immersion lens by Olympus. The model LUMFLN, has a numerical aperture (NA) of 1.1, and a working distance of 1.5mm. The series of two-inch lens, f_1 through f_5 are placed to re-adjust the beam size from 6.6 mm after the objective to match the different aperture sizes for the tweeter (4.4 mm) and the

woofer (15 mm). The pre-calibrated woofer and tweeter both are under open-loop control.

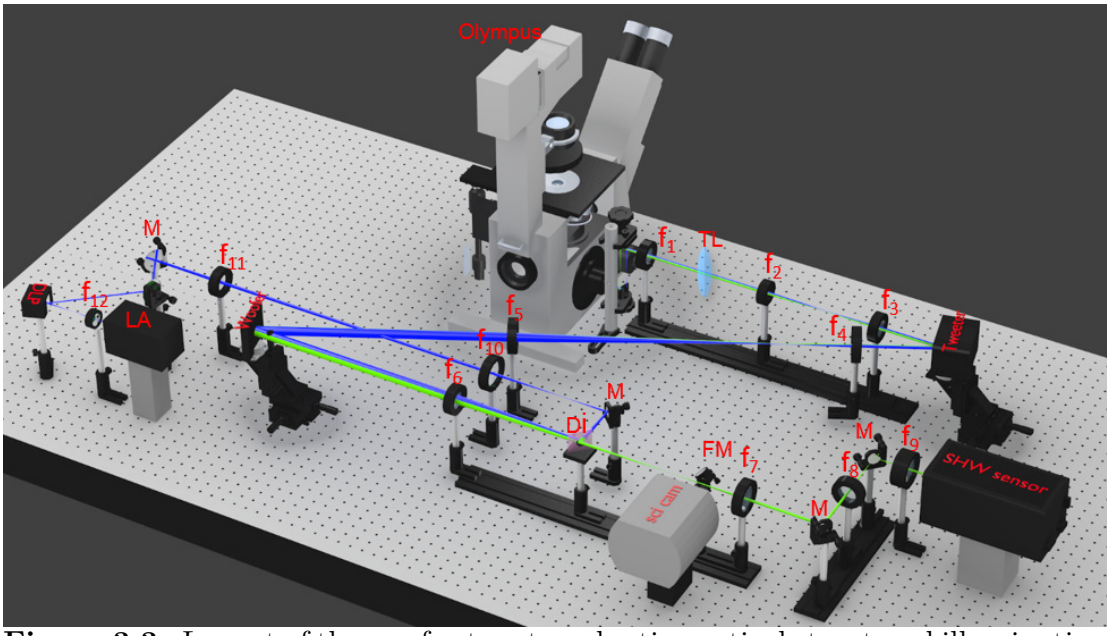

Figure 3.3: Layout of the woofer-tweeter adaptive optical structured illumination microscope. DLP: digital light projector. Sci cam: science camera. SHW: Shack-Hartmann wavefront sensor. Blue line: 488 nm excitation light path. Green line: emission path. M: mirror. The focal lengths of the lenses are: $f_1 = 120$ mm, $f_2 = 125$ mm, $f_3 = 120$ mm, $f_4 = 150$ mm, $f_5 = 500$ mm, $f_6 = 750$ mm, $f_7 = 150$ mm, $f_8 = 75$ mm, $f_9 = 100$mm, $f_{10}= 450$ mm, $f_{11}= 150$ mm, $f_{12}= 50$ mm. TL: trial lens (cylinder). LA: 488 nm Spectra-physics excitation laser. Di: dichroic mirror. FM: flip mirror.

3.5.1 Generation of SIM fringes

For generating fine structured light patterns in the focal plane, we refrain from using the traditional diffractive grating to generate the two beam interference patterns. This is because Equation 2.6 requires at least 3 rotational angles and at least 3 phase shifts of the SIM fringes for a total of 9 raw images per reconstructed image. Therefore, a diffractive grating is not the preferred method for generating SIM fringes as it introduces noise and latency into the system. The noise comes

from optical misalignment due to mechanical hysteresis, and the latency is due to the fact the one must wait for the grating to rotate and/or translate into position.

In a SIM microscope, the SIM illumination patterns can be generated with a digital light projector (DLP) [37, 57]. We do this our microscope, as indicated in Figure 3.3. We use the DLP3000 by Texas Instruments, with 608×684 micromirrors that can be switched in a binary fashion. The refresh rate for the micromirrors is 4kHz, and the input data bus for loading a binary matrix is 60-80MHz. To get the maximum SI spatial resolution at the focal plane, we set the DLP to 3 pixels per line.

The laser beam is spatially and temporally decorrelated by a spinning ground glass disk in front of the DLP to prevent speckle patterns.

Chapter 4

Application of the AOSIM Microscope on *in vivo* Samples

4.1 Introduction

In this chapter we discuss the implementation of a SIM microscope that includes the woofer-tweeter AO system. In the first section, we discuss the testing and characterization of the microscope. In order to verify that the system is diffraction-limited, we used fluorescent nano beads that were smaller than the theoretical resolution limit of a diffraction limited system. We also verified that the AO corrective system was working by inducing aberration with a trial lens. We conclude this chapter with a discussion of images acquired of a live Drosophilia embryo.

4.2 System characterization

The AOSIM system is characterized and tested by imaging 0.11μm fluorescent beads. With excitation light wavelength at 0.488μm, the diameter of the fluores-

cent beads are approximately half of the predicted diffraction limit predicted by Abbe, which is $\lambda/2\text{NA} \approx 0.22\mu\text{m}$. The diluted fluorescent beads are sandwiched between a slide and coverslip (No. 1.5). To simulate the effect astigmatism, we introduce a cylinder trial lens at the focal plane of f1 and f2, the common path of excitation and emission light. The induced aberration is conjugated to the back pupil of the microscope objective. To measure the wavefront, we turn a few DMD mirrors segments to the "on" state to selectively excite a bead in a small area. The wavefront of this "guide-star" is measured by the SHWS after adjusting the position of the flip mirror to direct light into this sensor.

From the measured wavefront, we analyzed the wavefront error up to the 22^{nd} Zernike mode. Error metrics include the RMS wavefront error, the peak-to-valley wavefront error, and the Strehl ratio [43, 24].The results of this characterization are found in Table 4.1.

Table 4.1: The table shows the peak-to-valley (P-V), Root mean square (RMS) and Strehl ratio of different AO configuration of our microscope setup. Emission wavelength: λ_{em}=0.515μm.

	No AO	Woofer (W)	Tweeter (T)	Both W, T
P-V (waves)	8.93	0.75	2.31	0.36
RMS (waves)	2.05	0.18	0.46	0.08
Strehl ratio	0.06	0.27	0.08	0.75

4.2.1 Adaptive optics correction

As shown in Figure 4.2a, due to the strong aberration introduced from the trial lens, without AO compensation, the images of the fluorescent beads are unresolvable. The corresponding reconstruction images using SIM, as shown in Figure 4.2 (e), also do not show any improvement. This is due to the fact that the aberration distorts the SI pattern in the focal plane, and the sample is no longer

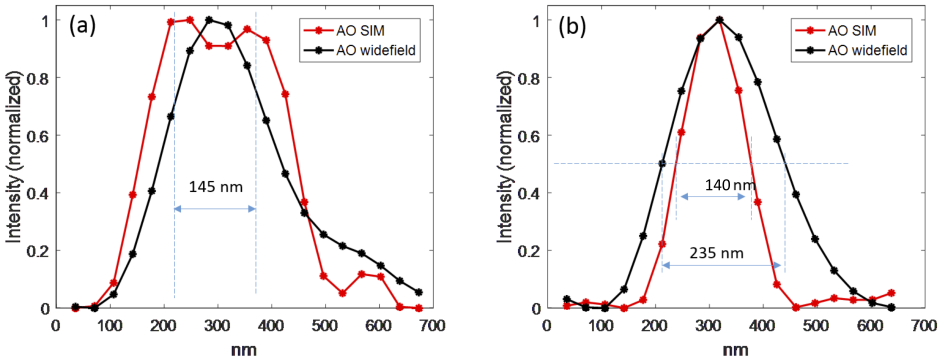

Figure 4.1: Comparison of 0.11μm beads under AO-Widefield (black line) and AO-SIM (red line). The intensity line profiles plot of the beads in the area 1, 2 of Figure 4.2 (d, h). (a) Intensity profile of two closely spaced beads. (a) The distance between two well resolved peaks in AO-SIM is 145 nm. (b) the FWHM of a single bead in widefield and AO-SIM are 235 nm and 140 nm, respectively.

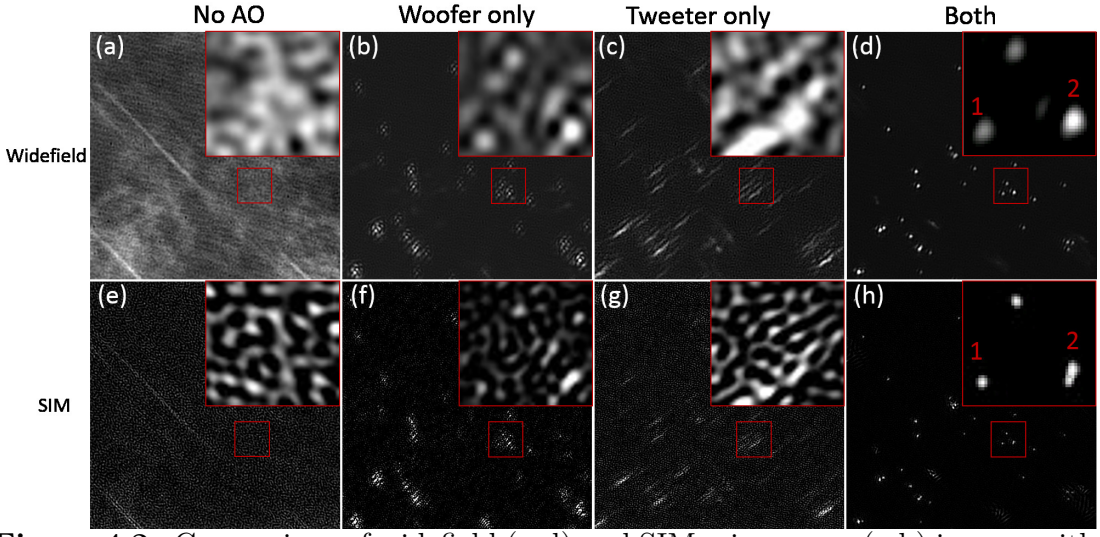

Figure 4.2: Comparison of widefield (a-d) and SIM microscope (e-h) images with and without wavefront correction. (a, e) Without AO. (b, f) Woofer only correction. (c, d) Tweeter only correction. (d, h) Both woofer and tweeter correction. The scale bar is 5μm. The intensity line profiles of the area 1, 2 in (d, h) are plotted in Figure 4.1.

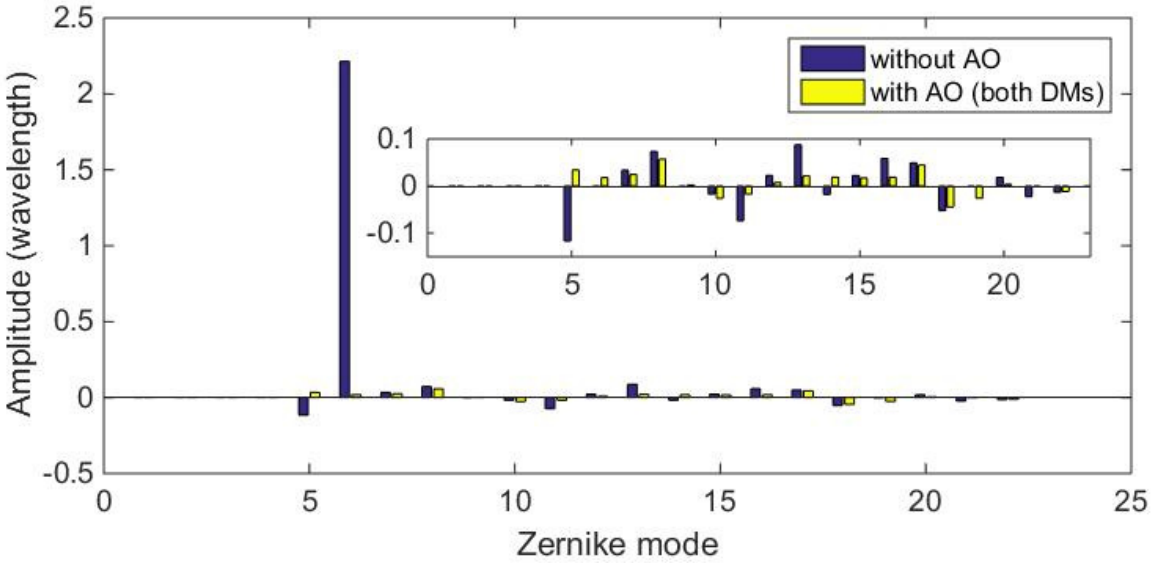

Figure 4.3: Zernike modes of the wavefront errors with and without woofer-tweeter correction. The inset figure is the value of the remaining Zernike modes after removing the big 6^{th} order vertical astigmatism. The Zernike order is in Noll single-index order [46].

illuminated by a well-defined SI pattern.

As shown in Table 4.1, without AO correction, the distorted wavefront of Figure 4.2a has a peak-to-valley wavefront error of 8.93 waves (5.9μm) and the RMS wavefront error is up to 2.05 waves. In this case, the Strehl ratio is only 0.06.

The values of the Zernike modes of the wavefront are shown in Figure 4.3. Zernike mode 6, which represents the vertical astigmatism induced by the trial lens is the dominant wavefront aberration. Note that the first four Zernike modes reflect piston, tip-tilt and focus, which are errors that do not require AO correction.

Figure 4.2b,f show images of 0.11 μm beads after using the woofer to compensate the low-order wavefront aberration (5^{th}-8^{th} Zernike modes). The signal-to-noise-ratio is significantly improved and the beads are visible in the images. As shown in Table 4.1, by compensating the low-order high-amplitude aberration,

the P-V wavefront error decreases from 8.93 to 0.75 waves. However, the resolution of the 0.11μm beads have not reached the diffraction limit, and the image quality is not improved using structured illumination. This is because we are only correcting the low-order aberration.

The residual aberrations, which have RMS wavefront errors around 0.18λ, limit the Strehl ratio to 0.27, which is much lower than the diffraction limited Strehl ratio of 0.8 [24]. If the tweeter only is used, the large amplitude aberration cannot be compensated, as shown in Table 4.1. This is a limitation imposed by the low stroke of the DM, which has a maximum stroke of 3.5μm. The residual aberrations still have P-V wavefront error around 2.31λ. The lower correction capability when using only the tweeter system leads to an RMS wavefront error around 0.46λ and a Strehl ratio that is only 0.06.

This limited correction capability of the tweeter-only setup can also be seen clearly in the images shown in Figure 4.2c,g. With wavefront correction from both the woofer and tweeter, as shown in Figure 4.2d, the wavefront error caused by the trial lens is corrected and the 0.11μm fluorescent beads are diffraction limited. After correction by the woofer-tweeter system, the P-V wavefront error is down to only 0.36λ and has a very low RMS wavefront error (0.08λ).

As shown in Figure 4.3, comparison of AO compensation with and without woofer-tweeter correction, most of the Zernike modes are dramatically decreased after AO compensation.

4.2.2 Super resolution

Figure 4.1 shows the line profile plot of areas 1 and 2 in Figure 4.2(d,h). After the SIM reconstruction, the two beads which are separated by a distance 145nm are resolvable. The size of a bead under widefield and AO-SIM is 235nm and

140nm, respectively. This confirms that the AOSIM microscope is able to resolve two beads that are separated by a distance less than the diffraction limit of the emission light. With AOSIM, the FWHM of a bead is decreased by a factor of 1.68×.

In this experiment, most of the aberration is compensated by the woofer-tweeter system. The Strehl ratio is increased from 0.06 up to 0.75. The correction capability of the woofer-tweeter system can be further improved by running the dual-DM correction system in a closed-loop control mode.

4.3 Imaging a live biological sample

We tested the AO-SIM imaging through a Drosophila embryo. The results are shown in Figure 4.4. Without AO correction (Figure 4.4a), the cell bodies and dendrites of the aCC and RP2 motoneurons are blurry. The aberration is mainly caused from the refractive index mismatch between the cover slip (#1.5 coverslip: R.I. 1.5), the mounting medium (Fluoreomount G: R.I. 1.4) and the sample. With dual DM compensation, the image in Figure 4.4b has improved resolution and the fluorescent signal is increased by 5 times in comparison with the image without AO correction (Figure 4.4e. Furthermore, using the SIM method, the red line in Figure 4.4e shows that the detailed structure of the dendrites sprouted from the axon [46] is well resolved.

4.4 Discussion

We have demonstrated that the combination of woofer-tweeter adaptive optics and structured illumination microscopy can correct high-amplitude low-spatial frequency and low-amplitude high-spatial frequency wavefront aberration and pro-

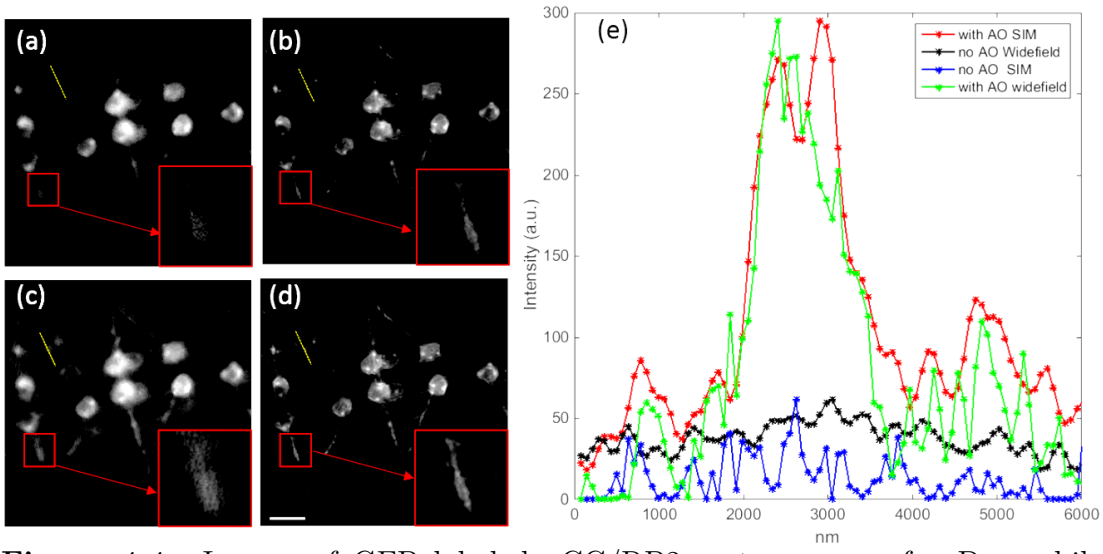

Figure 4.4: Images of GFP labeled aCC/RP2 motoneurons of a Drosophila embryo. (a) Widefield without AO. (b), SIM without AO. (c) Widefield with AO. (d) SIM with AO. (e) Plots of line profile in the (a-d). The scale bar is 10μm.

vides high-contrast high-resolution images. The experimental results showed that the system can correct large aberrations. When compared to the widefield microscope, the SIM method allowed two beads that are separated by 145nm to be resolved, giving a 1.62× super-resolution factor. The resolution improvement is a bit lower than the ideal case of 2×. There are two main reasons for this result.

The first reason is that the SIM fringes in the image plane are generated from direct projection of the DMD pattern. Here the contrast of the strip in the image plane degrades as the spatial frequency of the light approaches the cut-off frequency of the objective lens. In our experiment, we use an objective lense that corresponds to 0.8x of the cut-off frequency of the system. Using a high NA objective lens (NA=1.4, oil immersion), the resolution of the AOSIM system can be further improved, with a trade-off between resolution and working distance.

The fact that the AO corrective elements are conjugated to the pupil plane is also problematic. The pupil plane is the Fourier dual of the image plane. Since the Fourier dual of the SIM fringes are a pair of impulse-like delta functions at

the pupil plane, AO correction is all but impossible on the excitation path for the two beam interference phenomena. The result of this is that the degradation of the SIM fringes in the image plane due to aberrations cannot be corrected with AO. In Chapter 6 we discuss a method for correcting the wavefront aberrations on the excitation light path of a SIM microscope.

Lastly, since the correction field of view (isoplanatic patch) depends on the sample, the correction we applied is only valid within this area. If the aberration varies slowly within the sample (i.e. has a large isoplanatic patch), with our large field of view, a correction field of view (60μm $\times$ 70μm) is possible. In Chapter 5 we introduce a method for overcoming the limitation of the isoplanatic patch being too small in a densely labeled sample with wide variations in wavefront aberration.

Chapter 5

A Novel Scanning SIM Method

5.1 Introduction

Recently, a new SIM-based method of microscopy that incorporates two-photon excitation (TPE) has been implemented [62]. In this method, called scanning SIM, illumination patterns are scanned onto the object plane. In that work, the authors use a TPE method with an intensity modulation that emulates a sinusoidal pattern in the object plane. Emission light from the sample is then collected through both a photo-multiplier tube (PMT) and a CCD array. An image is built up by summing individual contributions from the excitation light.

The price to pay when using this technique is that it is slow when compared to conventional SIM. In conventional SIM, a typical setup requires 9 widefield images for a single reconstruction. If an image is to be built up into $N \times N$ pixels, then the number of PMT readings is increased by a factor of N^2. If one were to attempt to reduce the image acquisition time for scanning SIM, the N^2 factor would be a good place to start. Faster scanning SIM utilizes widefield imaging with a CCD array. TPE scanning SIM has been implemented in [64], with widefield image acquisition. Later on, the same group, went on to build a TPE scanning SIM

microscope which used a pinhole array coupled with a microlens array [63], a setup which allowed several excitation spots to be imaged at once.

Scanning SIM is attractive because the PSF of the microscope is contained within a small region in the object plane, which opens up the technique to adopting AO. In this study, we propose an alternative way to build up the scanning SIM illumination pattern that is both fast and suitable for AO. With the phase retrieval algorithm given in [17], we can create a multi-spot PSF in the object plane by using a spatial light modulator (SLM). We propose a TPE microscope since it rejects out of focus light, reduces photo bleaching and photo-toxic effects, and is good for optical sectioning. We also propose a multi-spot PSF in order to speed up the imaging process. We simulate an illumination pattern that is suitable for a SIM reconstruction with TPE. Furthermore, since the multi-spot PSF is contained within a small region in the object plane, we can use adaptive optics to make local wavefront corrections within the sample. This will allow SIM to be used in deep tissue imaging.

The rest of this chapter is organized as follows. In Section 5.2, we discuss the mathematical framework of SIM, and also method of obtaining our simulations. In Section 5.3, we discuss the results of our simulations, as well as the implications for using this method for scanning SIM. We conclude with Section 5.4, with a summary of the present work and discussion of future work.

5.2 Simulation Framework

Conventional SIM is usually a widefield microscopy technique. The robustness of the reconstruction depends on the fidelity of the illumination patterns (cf Equation 2.2). That is to say, any deviation from the ideal sinusoidal illumination pattern, the spectral leakage in the frequency domain will degrade the reconstruction,

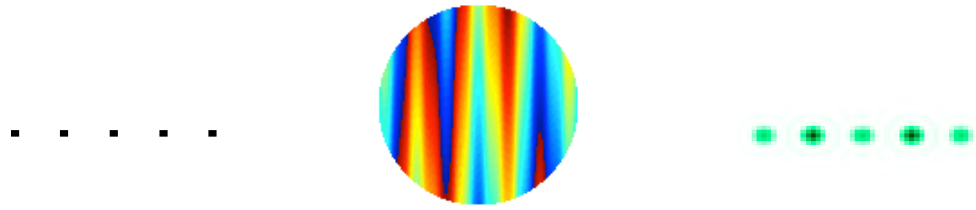

(a) Target PSF 1 **(b)** Phase solution **(c)** PSF in object plane

Figure 5.1: Non-ideal proposal PSF for multi-spot scanning SIM. The five dots in the target PSF are close enough that coherent interference distorts the intensity of each spot in the object plane.

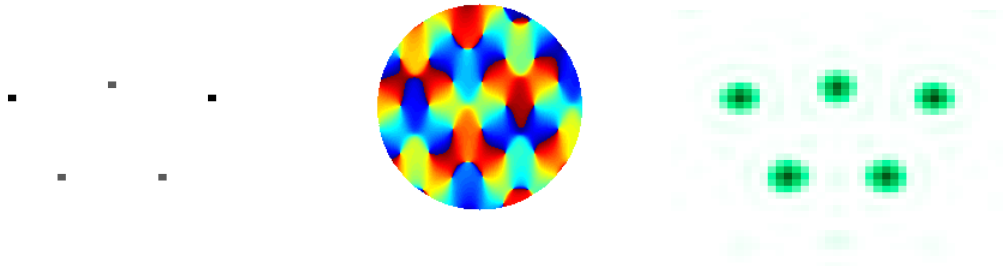

(a) Target PSF 2 **(b)** Phase solution **(c)** PSF in object plane

Figure 5.2: A better proposal PSF for multi-spot scanning SIM. By using an offset in the vertical direction, coherence is no longer a problem in the object plane. The offset is not an issue after scanning this PSF through the object plane.

since Equation 2.5 will be violated. Therefore, a clean, high-contrast illumination pattern is essential for a successful SIM reconstruction. Another source of error in SIM reconstruction is an incorrect estimation of phase and spatial frequency of the illumination patterns. In this chapter, we estimate the spatial frequency using Fourier domain techniques. Phase can be estimated using an autocorrelation maximization routine, as in [32].

Pattern projection onto the object can be challenging in and of itself, but when imaging deep into a sample, aberrations blur the illumination pattern, making SIM reconstruction difficult. Use of Adaptive Optics (AO) can help, but wavefront

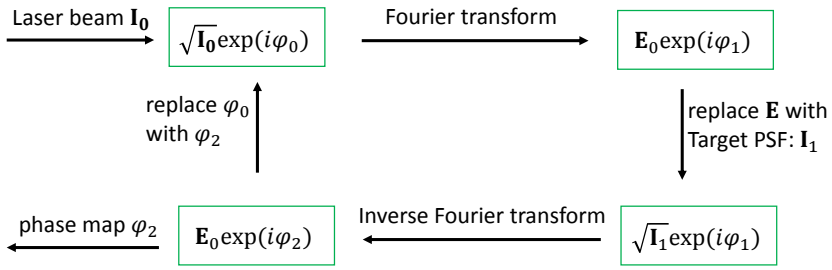

Figure 5.3: Block diagram of the iteration step of Gerchberg-Saxton algorithm for phase retrieval.

correction is limited to a small area known as the isoplanatic patch, which typically does not cover the entire field of view [31]. For a typical image of a drosophila embryo, the isoplanatic patch has been found to be around 20μm [55]. Therefore, we aim to keep our PSF contained within a region of this size in the object plane.

In two-photon excitation (TPE) microscopy, the excitation light is focused into a small volume in the object plane, similar to a confocal laser scanning microscope. The theoretical PSF of a single photon confocal system is modeled by a Bessel function of the first kind [19]. The TPE system is nonlinear, and its PSF is proportional to the square of the intensity of the single photon PSF [49]. Therefore, our multi-spot PSF must be squared in our simulations.

We use the Gerchberg-Saxton phase retrieval algorithm from [17], implemented in Matlab. We begin by proposing a desired PSF that meets our requirements for scanning SIM. Next we perform the phase retrieval algorithm to derive a phase distribution for the SLM. We then generate a PSF from the phase distribution in order to emulate the scanning operation in software. Figure 5.3 shows a block diagram of the iterative loop. In a typical SIM reconstruction, there are three phases of illuminations patterns, and at least two rotations. With our method, the illumination pattern can be phase-shifted by changing the scanning path with galvo mirrors. Likewise, to rotate the illuminate pattern, the SLM distribution

can be rotated, and the beam steered accordingly.

5.3 Results and discussion

To illustrate the simulation process, we propose a multi-spot PSF as shown in Figure 5.1. The proposed PSF is simply an array of five points arranged in a linear fashion. In making this proposed PSF, the hope is that the derived phase map would produce a set of points that have an even intensity distribution. In Figure 5.1c we can see that this is not the case. If we were to use this generated PSF for a scanning SIM reconstruction, the illumination pattern would be roughly sinusoidal, but with additional frequency components that make the pattern unsuitable for a SIM reconstruction. The uneven intensity distribution among the five spots is likely a result of coherent interference of the laser source. Thus, a better proposed PSF should increase the distance between the points so that coherent interference is decreased.

In order to create a more even distribution among the PSF spots, some spacing should be added in between the pixels in the proposed PSF. This is what we see in Figure 5.2a. We add some offset in the vertical direction in order to mitigate the effect of coherent interference. We can also weight the different points in the proposed PSF so that the intensity distribution of the generated PSF is more uniform. The offset in the vertical direction of the proposed PSF introduces an asymmetry, but this will not be an issue due to the scanning operation. In fact, we can illustrate this point by simulating this very operation. In Figure 5.4, we can see a small sample of the effective illumination pattern by scanning the generated PSF from Figure 5.2c. It is apparent that this illumination pattern is very close to sinusoidal, although there is a ghosting effect due to the presence of side lobes. In practice, this effect will not be present since the illumination pattern can be made

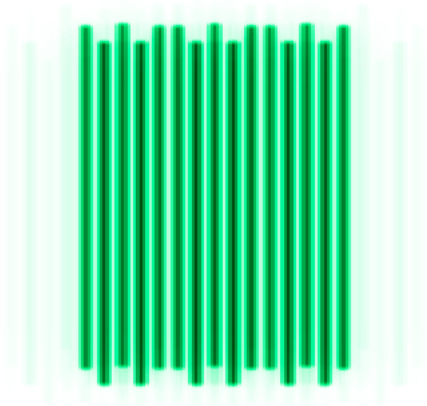

Figure 5.4: Illustration of scanning SIM using a multi-spot PSF. The PSF here is a 2D scan of Figure 5.2c, obtained from the phase pattern shown in Figure 5.2b.

arbitrarily large by the scanning operation. We can scan an area that is larger than the region of interest, and then crop the SIM images before performing the SIM reconstruction algorithm.

In Figure 5.5, we show the 1D Fourier representation of our 2D sinusoidal pattern. If our generated pattern were truly sinusoidal, then only the peaks present at $\pm\pi/3$ would be present. However, we note that noise is present in the areas denoted by the red ovals. In practice, we would continue to refine the multi-spot PSF using the phase retrieval algorithm to come up with a better PSF.

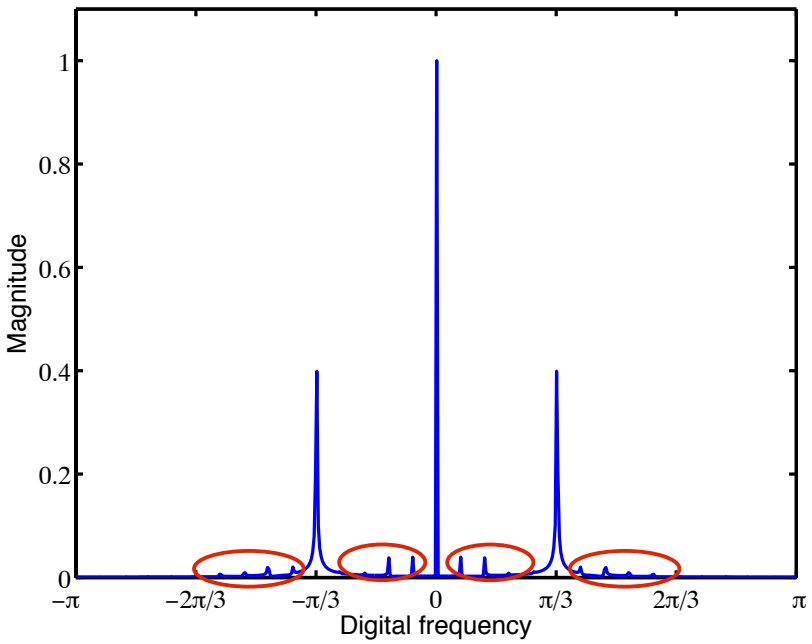

Figure 5.5: The Fourier domain representation of the illumination pattern obtained by the multi-spot scanning SIM method. The conventional SIM illumination patterns would only contain the peaks at frequencies $\pm\pi/3$, and 0. Here, the spectral leakage is noted by the red ovals. In principal, the phase-retrieval algorithm could produce a multi-spot PSF whose sinusoidal scanning pattern is arbitrarily close to the ideal sinusoid.

In Figure 5.6, we illustrate a SIM reconstruction. The test image (Figure 5.6a) is blurred with the PSF of the microscope system and with white noise at 20% of peak image intensity (Figure 5.6b). The simulation shows a robust reconstruction of the TPE scanning SIM method even when noise is added to the SIM images in the frequency domain (Figure 5.6c). The robustness is in part due to the normalizing effect of the Wiener filter that is part of the SIM reconstruction algorithm. It is also due to the apodization function that we apply to the final image. In either case, the present work has shown that the conventional SIM reconstruction algorithm can be applied to the images obtained with the TPE scanning SIM method.

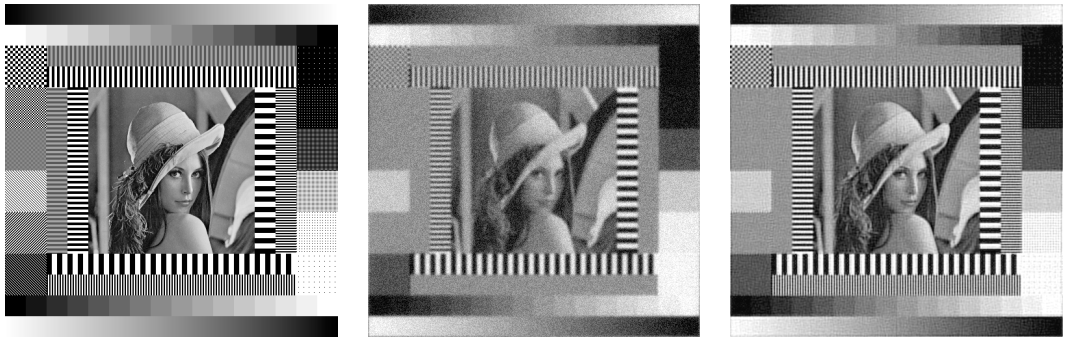

(a) Ground truth **(b)** Blurred image with noise **(c)** Reconstruction

Figure 5.6: A demonstration of the reconstruction with our method. Image (a) is the ground truth image, from [32]. Image (b) is what would be visible with a conventional, widefield microscope: the image is blurred with the PSF of the microscope, and white noise is added at 20% of peak image intensity. The SIM reconstruction (c) is shown using the TPE scanning SIM pattern obtained in this section.

5.4 Conclusion

In this chapter we simulated a scanning SIM reconstruction method based on PSF shaping in the object plane. The PSF was constructed with a phase retrieval

algorithm, which in turn generated a real PSF in the object plane. This generated PSF can be written into in the object plane of a microscope with a spatial light modulator. The PSF is large enough to offer an increase in the speed of scanning SIM, yet small enough to be fully contained within an isoplanatic patch in an AO system. We plan on carrying out this work in a TPE microscope with adaptive optics for obtaining SIM reconstructions in thick, densely labeled samples, such as in a drosophila embryo.

Chapter 6

Emission and Excitation Light Paths in SIM

In this chapter, we introduce a framework for modeling the wavefront aberrations of both excitation light and emission light within the context of SIM imaging. We show that in some cases, AO correction is sufficient on the emission path of light alone, while in other cases it will be necessary to add AO correction on the excitation path of light. We use Fourier optics theory to model the two-beam interference that is utilized to SIM pattern generations. We use the Fourier beam propagation method to model the two beams of light as they leave the back aperture of the microscope and interfere coherently at the focal plane in the sample. We model aberrations on the back aperture of the microscope as linear combinations of Zernike polynomials. This method allows us to model phase aberrations present in both the excitation and emission light paths. We choose the Zernike mode representation for aberrations since it is widely used in AO corrective systems. The simulation framework also suggests that the AO correction for the emission light should be conjugated to the back aperture of the microscope, rather than the pupil plane (as is typical).

The rest of this chapter is organized as follows: In the next section, we discuss the generation of the SIM illumination patterns with the two-beam interference phenomena. In the next section, we discuss the simulation framework, which operates in the context of SIM illumination pattern generation under wavefront aberrations modeled by Zernike polynomials. The framework discussion also includes the method of Fourier beam propagation for modeling light traveling in the forward excitation path, and also the autocorrelation of the pupil function to represent the light interaction with the OTF in the emission path. In the Results section, we show the simulations. We conclude with a discussion of our results, along with a proposed method for wavefront correction on excitation light for SIM fringes. At each step, the accompanying code is referenced in Appendix A.

6.1 Generation of SIM fringes

To begin this chapter, we revisit the generation of the SIM fringes in the image plane. For clarity, some of the figures from Chapter 3 are repeated here. SIM fringes are generated in the image plane by the two beam interference phenomena of a diffractive element in the excitation light path. The emission light path is that which leaves the sample at the image plane and is directed toward the science camera for imaging. In the next sections we discuss excitation and emission light, each in its own right.

6.1.1 Excitation light

For a SIM microscope, the DMD is placed on the optical path such that the DMD and the image of the sample are optical conjugates. Therefore, if we desire to have a spatial sinusoid illumination pattern at the image plane, then a spatial

sinusoid must be present at the DMD plane. In reality, it is impossible to have a spatial sinusoid at the DMD, because its micromirror locations are discrete, and each micromirror "state" is binary; it can only be in the "on" or "off" state. Therefore, the best we can do is to project a square wave onto the DMD. Figure 6.1 illustrates this discrete "square wave" pattern on the DMD.

The discrete nature of the DMD notwithstanding, it is possible to obtain a sinusoid at the sample, given a square wave at the DMD. If we examine the Fourier series representation of a square wave (Equation 6.1) we can see that the fundamental frequency dominates in magnitude, and that a low-pass filter would effectively null out the harmonics.

$$f(x) \propto \sum_{\substack{n \text{ odd}, \\ n>0}}^{\infty} \frac{1}{n} \sin n\pi x \tag{6.1}$$

Conceptually, this argument carries over to the DMD as follows: If the pitch of the DMD square wave pattern were close to the diffraction limit, then the low-pass filtering action of the microscope can diminish the magnitude of the harmonics embedded in the signal. However, an optical intensity signal deviates from the Fourier series representative of an ideal square wave in that the intensity is never negative. That is, the DMD produces a signal that is not centered at "zero" units of illumination intensity. We can compensate for this by adding a constant "DC" offset term for the Fourier series representation. In the optical domain, we remove the "DC" term by blocking the zero order diffractive ray, as seen in Figure 6.1.

6.1.2 The pupil plane

It is widely known that the lens is a Fourier transforming device under certain circumstances. In [18], the author demonstrates mathematically that a converging

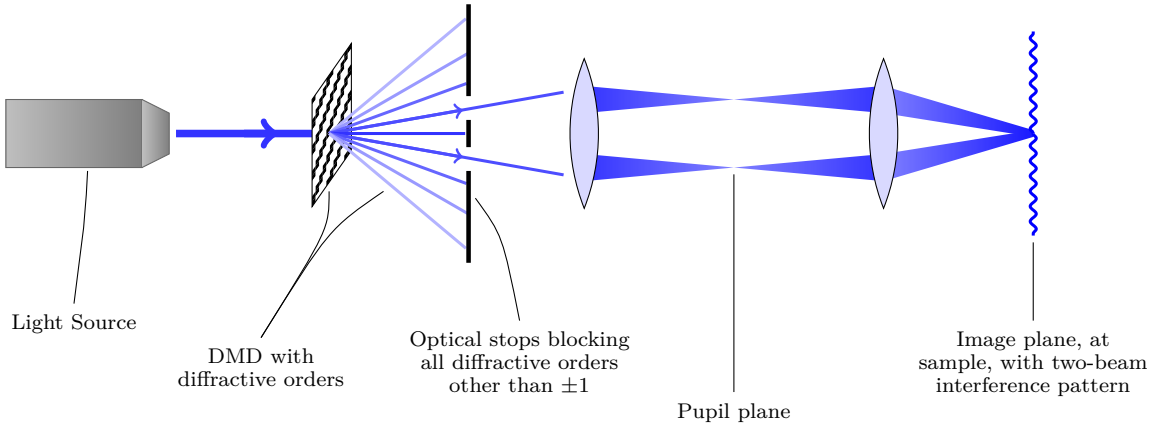

Figure 6.1: Diagram explaining the excitation light path. The excitation light is shown in a blue color because our microscope uses a 488nm laser light source, which is in the blue region of visible light.

lens with a focal length f, operating on coherent light emanating from an object at distance d, has field distribution U_f at the focal plane given by

$$U_f(x,y) = \frac{A\exp\left[j\frac{k}{2f}(1-\frac{d}{f})(x_f^2+y_f^2)\right]}{j\lambda f} \times \iint_{-\infty}^{+\infty} t_o(x_o,y_o)\exp\left[-j\frac{2\pi}{\lambda f}(x_o x_f + y_o y_f)\right] dx_o dy_o \tag{6.2}$$

with the amplitude transmittance of the object given by t_o. In a microscope, f is the image plane, and d represents the pupil plane. Note that the quadratic term vanishes ($e^{1-\frac{d}{f}} = 1$) when $f = d$. In other words, the image at the pupil plane is the Fourier transform of the image at the focal plane, up to a constant multiple.

Consider now the Fourier dual of a spatial sinusoid, which is a pair of delta functions in the reciprocal space, with locations $\pm(k_x, k_y)$. A perfect delta function is defined over a support of measure zero. However, a spatial sinusoid whose frequency is near the diffraction limit of the microscope will have a Fourier representation which includes some spectral content that leaks into a non-empty neighborhood around the points $\pm(k_x, k_y)$ in reciprocal space.

Nonetheless, this neighborhood is small. It is especially small when compared to a wavefront corrective device. In fact, it is all but impossible for a AO device to correct the wavefront of the spatial sinusoid if the AO device is conjugated to the pupil plane.

In the following sections we show the effect of wavefront aberrations on both excitation light and emission light in a SIM microscope. We develop a simulation framework that can be used to show how AO correction of wavefront aberrations emission light path differs from that of excitation light. In an AO microscope, the AO corrective elements are typically conjugated to the pupil plane, since it is this plane where the entire wavefront can be projected onto a wavefront sensor and a deformable mirror.

Given the discussion in this section, we know that this practice is insufficient for correcting wavefront aberrations on excitation light. Therefore, a SIM microscope, with the typical AO pupil plane conjugation, will be unable to create good SIM illumination patterns in the sample, in the sense that the spatial sinusoid will be distorted (k-space vector components moved or smeared) and the illumination intensity will not reach full depth.

6.2 Simulation framework

Here we introduce the simulation framework for this study. The light fields that cause the two-beam interference patterns present in SIM are represented as complex exponentials with wave number k based on the wavelength of light, in this case 488nm. The electric field E is obtained by creating a matrix

$$E = \exp(i \sin\theta \cos\alpha \, k_x \mathbf{x} + i \sin\theta \sin\alpha \, k_y \mathbf{y} + i \cos\theta \, k_z) \tag{6.3}$$

with azimuthal angle α on the objective lens (0, π), beam angle θ as defined by the numerical aperture of the objective lens (in this case, NA=1), and k the wave number with x, y, and z components. The direction of propagation in the z direction.

With this representation of the EM fields for both beams, we can mathematically obtain the two-beam interference pattern by decomposing the fields into their polarized components and adding pair-wise. The Matlab implementation of this operator is in Appendix A.3. To obtain the real-valued intensity of the field, I, the x, y, and z components of E are multiplied by their complex conjugates and then summed[1]:

$$\mathbf{I} = \sum_{n=x,y,z} E_n \cdot E_n^* \tag{6.4}$$

To represent the propagation these electromagnetic fields from the objective lens into the sample, we note that the distance travelled can be represented by a number oscillations of the field. In other words, we have a phase delay, which can be represented in the Fourier domain with a complex exponential:

$$\mathcal{F}\{\mathbf{E}\} \cdot e^{ikz_0} \tag{6.5}$$

with the result of having traveled a distance of z_0-nm being the inverse Fourier transform of Equation 6.5. We can now obtain the two beam interference pattern with Equation 6.4 which gives us the SIM fringes in the object plane.

To address the field aberrations, we can adjust our model so that the initial electric field is scaled by a subset of the pupil function, which is in turn has a Zernike polynomial representation. Wavefront aberrations are induced by the sample and coverslip/mounting media index of refraction mismatch; these aberra-

[1]See code snippet A.1 for implementation details.

tions are in fact variations of the optical path distance (OPD) on a cross section of the beam as it travels from the objective lens to the focal plane in the sample. Using Zernike polynomials is a convenient way to capture the OPD variation across the beam for reasons discussed above.

We choose the simulate the aperture of the objective lens as a large Zernike polynomial with a matrix of 2048x2048 pixels with a circular subset showing the active portion of the back aperture of the objective. The two interfering beams are represented as subsets of the aperture matrix with radially opposing locations (as in Figure 6.2), with a size of 256x256 pixels, and an offset from the edge of the aperture matrix by 40 pixels. In this way both the aperture and the two interfering beams are represented by Zernike polynomials in a way that is faithful to actual SIM techniques. Additionally, the sizes of the image matrices are "five-smooth" numbers[2], which is useful for the run-time of the Fast Fourier Transform.

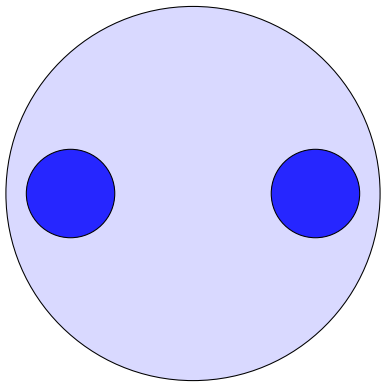

Figure 6.2: The aperture plane of the microscope: This figure shows the lens (light blue) and the two beams of coherent light (dark blue) that meet in the sample to form SIM illumination patterns. The two beams are near the edge of the aperture. The closer to the edge, the higher the spatial frequency of the SIM illumination patterns in the image plane. If two beams are too close to the edge, then the spatial frequency will be too high because of the low-pass filtering effect of the microscope.

[2]Five smooth number: a number whose prime factors are not larger than 5.

Having produced the two-beam interference patterns in the sample by Equation 6.4, we can now simulate the effect of emission light under the effect of the OTF. There are two ways to simulate the OTF of the microscope. One of which is to calculate the Fourier dual of the PSF. This involves either theoretically calculating the PSF given the wavelength of light and the photonic qualities of the beam (single photon vs multi-photon laser source), or measuring the PSF directly on a diffraction limited object.

The other way to obtain the OTF is to use the autocorrelation of the pupil function. In our case, since we have already represented the pupil function as a linear combination of Zernike modes, we use this second method. In a sense, we get the OTF "for free" using our framework. Additionally, if we calculate the OTF with this method, we can treat wavefront aberrations as part of the system. Using this pupil-function-derived OTF, we are are able to simulate the effect that the aberrations have on the SIM fringes in the focal plane. If the SIM fringes do not hit full modulation depth, then the frequency heterodyning effect is not as strong, because Equation 2.2 is violated.

Furthermore, we can show the deviation of fully under the OTF of the microscope, and in this way obtain a simulation of the image which the science camera observes of the SIM fringes under both excitation and emission aberrations.

The OTF can be obtained with the autocorrelation of the pupil function as follows [18] [35]:

$$OTF = \mathcal{F}^{-1}[\mathcal{F}[P] * \mathcal{F}[P]] \tag{6.6}$$

Usage of the this OTF derivation that includes the Zernike representation of sample and system-induced aberrations is shown in Appendix A.6. This function is used to apply aberrations in two steps:

1. On the the excitation light path, a pair of subsets of the aberration function is applied to both of the excitation beams that provide the SIM fringes via two-beam interference patterns. These subsets correspond to the sections of the back aperture of the microscope upon which the two interference beams are projected.

2. On emission light path, the entire aberration function is applied to the pupil, thus modelling the widefield image capture of the sample with SIM fringes.

The framework can display any combination of Zernike polynomials by simply calling `getZernikeWeighted` with a list of weights. Usage of this code is demonstrated in Appendix A.4. The aberration matrix for a particular set of Zernike coefficients, (a set which corresponds to imaging the Clarity mouse brain in [46]) is shown in Figure 6.3.

Using the Zernike polynomial representation of wavefront aberration, the framework can display and simulate the effect of an arbitrary aberration function using a linear combination of zernike polynomials. Single coefficients can be selected to simulate, for example, astigmatism, trefoil, defocus, or tilt only. Since the zernike polynomials are orthogonal on the unit disk, the linear combinations different coefficient arrays form a complete representation of any aberration.

Different windowing functions can be added so that the discrete Fourier transform algorithm's implementation does not cause aliasing or spectral leakage due to the implicit windowing function action caused by using square matrices for computation.

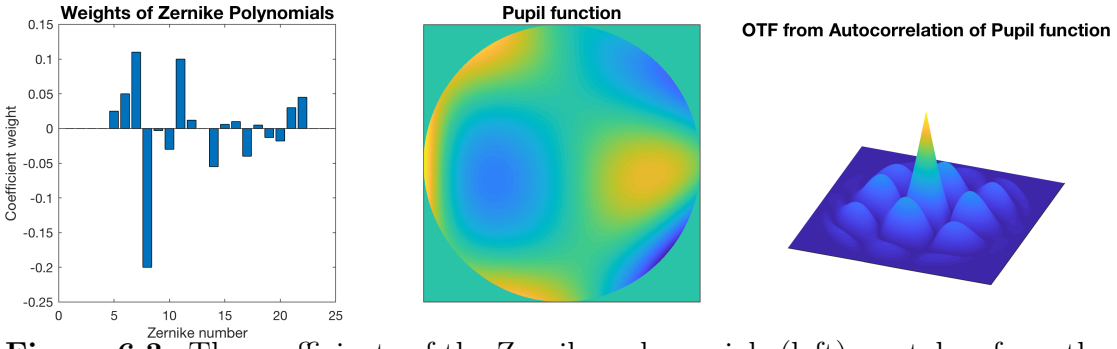

Figure 6.3: The coefficients of the Zernike polynomials (left) are taken from the work in [46], where the CfAOM group imaged the "Clarity" mouse brain at a depth of 500μm. The center pane shows the simulated pupil function, given the Zernike coefficients at left. The OTF is shown at right.

6.3 Results

We used the simulation framework to show two different types of aberrations. One type, shown in Figure 6.4 consists of low-order, low-magnitude aberrations in terms of Zernike bases. Figure 6.4(e), we see that the SIM fringes visible at the science camera have a good modulation depth, and are rotationally aligned with the azimuthal angle, which in this case corresponds to a "vertical" alignment.

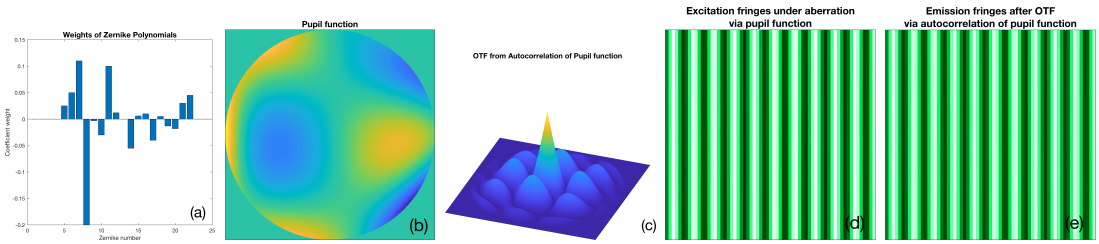

Figure 6.4: SIM fringes visible under the excitation light path and emission light path. (a) shows the Zernike coefficients in the Clarity mouse brain imaging system from [46], along with the associated pupil plane (b) and the OTF (c). In (d) we observe that the effect of aberrations in the excitation light on the SIM fringes.

On the other hand, in Figure 6.5 we see the simulation of high-magnitude aberrations. This figure shows that the SIM fringes in the sample are in a different azimuthal orientation (d), which was calculated to be 1.4°, when in fact it should

have been 0°. Figure 6.5(e) shows that the fringes under the effect of the OTF suffer from poor modulation depth. Naturally, this is bad for both super-resolution and sectioning SIM. The high magnitude aberrations are seen to change the location of the delta function in reciprocal space, which causes difficulties in the SIM reconstruction. Under the effect of the OTF, we can see weak modulation depth, which inhibits the spatial frequency mixing effect upon which the super-resolution SIM reconstruction is based.

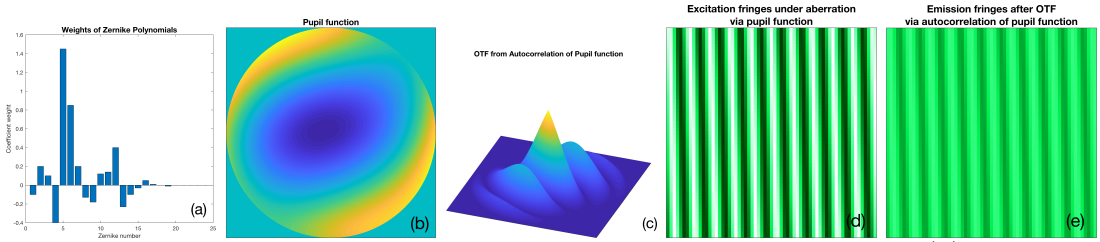

Figure 6.5: SIM fringes with aberration on the excitation path. (a) shows the Zernike coefficients that were used to produce the aberration, while (b) shows aberration function at the pupil plane. (c) shows the OTF calculated by the method discussed in this section. The fringes in (d) are what would be imaged at the sample. The angle of the SIM fringes in the excitation light path was calculated to be 1.4°, when in reality it should be 0°. (e) shows what the SIM fringes would look like at the science camera, where the modulation pattern does not reach full depth.

In terms of AO correction, most AO systems will be successful in correcting for the OTF of the microscope, since the AO correction is conjugated to the pupil plane. This will correct for the poor modulation depth seen in Figure 6.5(e). However, the change of azimuth angle will not be addressed by this AO correction. In fact, there is a whole class of aberrations for which the excitation fringes undergo degradation. This is because the typical AO setup for microscopy places the corrective element at a plane that is conjugated to the pupil plane. However, the pupil plane is the Fourier dual of the image plane, and the Fourier dual of the SIM illumination patterns are point-like.

A better SIM system will place another AO correction on one of the interfer-

ence beams at a plane that is conjugated to an aberrating layer[3]. It is sufficient to have correction on a single beam, not both. This is because the two-beam interference effect arises from mutual phase coherence. Therefore, it is sufficient to match the wavefronts so that they are phase-coherent, rather than require a perfectly corrected wavefront on both beams. The precise location of the corrective element should be conjugate to an aberration plane in the sample, if that plane is known. AO systems in both astronomy and microscopy have be developed in multiconjugate AO. Correction for the wavefront in the detection path should be implemented as required by the biological tissue or sample.

6.4 Conclusion

In this chapter we used the framework that was developed at the CfAOM in order to demonstrate the effects of aberration on the excitation and emission light paths. Most treatments of AO for SIM microscopes gloss over the fact that AO elements that are conjugated to the pupil plane of the microscope are not able to correct for wavefront aberrations when light is traveling *into* the sample. This is because at the pupil plane, the the Fourier dual of the SIM illumination patterns are contained within a very small area of the total plane.

We use the Zernike polynomial model to simulate the wavefront aberrations present at the pupil plane. We use Fourier beam propagation technique (FBP) to simulate the effective SIM pattern in the image plane. We do this for various Zernike modes and their combinations to show that for certain modes if sample-induced aberrations are not corrected in the excitation path, then no amount of wavefront correction on the detection path is worthwhile.

[3]this was propose in [39] but it has not been implemented in this context, i.e. as a way to get better SIM patterns via AO correction on excitation light.

In this work we also showed that in addition to being able to disregard certain modes of aberration, other modes can be effectively corrected by placing an AO wavefront correction in between the aperture plane and the pupil plane. Furthermore, it is not necessary for the corrective element to span both of the interference beams; it suffices to shape the wavefront such that the aberration in one beam exactly matches the wavefront of the other. This is sufficient for the two-beam interference phenomena to occur.

Chapter 7

Conclusion

In Chapter 1 we introduced the need for SR microscopy that is paired with AO for biological imaging, and posited that SIM is a good solution for biologists, given that it enables *in vivo* imaging of biological samples.

In Chapter 2 we discussed the SIM Framework, including the mathematics that drive the imaging system, along with the reconstruction techniques.

In Chapter 3 we discussed the SIM microscope that was designed in the Center for Adaptive Optical Microscopy at the Joel Kubby lab here at UCSC.

In Chapter 4, we report on the details of characterizing the SIM AO microscope, including the design and placement the AO elements for reducing sample and system-induced aberrations. We also present images of a zebrafish embryo showcasing the merits of the SIM microscope.

In Chapter 5 we discussed a novel technique for improving SIM by scanning the illumination fringes into a sample. The scanning pattern proposed would be an alternative way to illuminate the sample with SIM fringes using a scanning operation with a two-photon excitation light source. This method would work well with adaptive optics since the scanning pattern is small enough to be completely enveloped in the isoplanatic patch of the AO correction. The phase mask to

be applied to the SLM was obtained by the Gerchberg-Saxton phase retrieval algorithm.

In Chapter 6 we discussed some considerations for improving an AO system for a SIM microscope. Most AO systems place the corrective element conjugated to the pupil plane of the microscope. For a SIM microscope, the excitation light is confined to two small "impulse"-like points, which is the Fourier dual of the SIM fringes in the image plane. The proposal discussed in this chapter would place the corrective element in a plane where the excitation light can be corrected for aberrations in the excitation light path. Aberration on the emission path can be corrected in the typical fashion by conjugating an AO corrective element to the pupil plane. We also discussed the mathematical framework used to simulate this system and derive these results.

Appendix A

Code snippets

A.1 Two-beam inteference pattern

This code snippet illustrates how to create two beam interference patterns in the image plane of the SIM system. It uses function that are defined elsewhere in the code base, and whose implementations are given further below.

```
%% Create the two beams
% beam angle is defined from the numerical aperture of objective lens.
theta_nn1 = asin(NA/nn1);% angle in water;  snell's law;
theta1_beam1 = theta_nn1;
theta2_beam2 = theta_nn1;

offset_angle = 0;
alpha_beam1 = (offset_angle + 0)*pi/180;        %azimuthal angle of beam 1
alpha_beam2 = (offset_angle + 180)*pi/180;      %azimuthal angle of beam 2

% rotation theta around y
Yrot_beam1 = rot_y(theta1_beam1);
Yrot_beam2 = rot_y(theta2_beam2);

% rotation alpha around z
Zrot_beam1 = rot_z(alpha_beam1);
Zrot_beam2 = rot_z(alpha_beam2);

% polarization state of beam after rotation
Polari_beam1 = Zrot_beam1*Yrot_beam1*select_polar(beam_1);
Polari_beam2 = Zrot_beam2*Yrot_beam2*select_polar(beam_2);

EM_beam_1 = EM_field(theta1_beam1,alpha_beam1,k,x,y,z);
```

```
EM_beam_2 = EM_field(theta2_beam2,alpha_beam2,k,x,y,z);

function y=select_polar(x)
    Px=[1 0 1/sqrt(2) 1i/sqrt(2)];
    Py=[0 1 1i/sqrt(2) 1/sqrt(2)];
    Pz=[0 0 0 0 0 0];
    y=[Px(1,x);Py(1,x);Pz(1,x)];
end
```

A.2 Electric field

This code is used to implements Equation 6.3. It returns the complex field components of a beam of light.

```
function y=EM_field(theta, alpha, k, xx, yy, z)
    % theta - beam angle, defined by numerical aperture of objective lens
    % alpha - azimuthal angle of beam propagation
    % k - wave number: 2*pi*n/lambda
    % xx, yy grid matrices
    % z - scalar
    y=exp(1i*k*(sin(theta)*cos(alpha)*xx+sin(theta)*...
            sin(alpha)*yy+cos(theta)*z));
end
```

A.3 Two beam interference

This code is used to implements Equation 6.4, returning individual field components that are later summed pairwise.

```
function [ Ix, Iy, Iz ] = ...
    interferenceTwoBeams( EM_beam_1, EM_beam_2, Polari_beam1, Polari_beam2 )
    %INTERFERETWOBEAMS %% Decompose and add components pairwise
    % Account for polarization using function 'Polari_beam
    %   The electric fields are added pairwise, scaled by polarity.
    %   The intensity of the x, y, and z components of the resultant wave
    %   are obtained as the square of the real part of the field

    Ex=Polari_beam1(1,1) * EM_beam_1 + Polari_beam2(1,1)   .* EM_beam_2;
    Ey=Polari_beam1(2,1) * EM_beam_1 + Polari_beam2(2,1)   .* EM_beam_2;
    Ez=Polari_beam1(3,1) * EM_beam_1 + Polari_beam2(3,1)   .* EM_beam_2;

    Ix=Ex.*conj(Ex);
    Iy=Ey.*conj(Ey);
    Iz=Ez.*conj(Ez);
end
```

A.4 Aperture function

The purpose of this code is to generate the aperture function as a linear combination of Zernike polynomials. It wraps the `getZernikeWeighted` function in a "for-loop". This snippet also shows the usage of the function. The coefficient array that get stored in the variable `coeff_array` shows what the aberration was for the Clarity mouse brain.

```
%% Declare an array of weights that correspond to the magnitude of each
%  Zernike mode. The coefficient array here represents the aberrations
%  present when imaging the Clarity brain.
coeff_array = [0,0,0,0,.025,.05,.11,-.2,-.003,-.03,.1,.012,0,-.055,...
    .006,.01,-.04,.005,-.013,-.018,.03,.045,0,0,0,0,0,0];

[num_zern_mode,~] = size(modes_zern);

%% Form the pupil functions as sums of Zernike polynomials
pupilFunctionsLarge = zeros(size_zern,size_zern,num_trials);
pupilFunctionsSmall = zeros(size_zernSmall,size_zernSmall,num_trials);
for trial = 1:num_trials
    for polynom = 1:num_zern_mode
        n = modes_zern(polynom, 1);
        m = modes_zern(polynom, 2);
        weight = coeff_array(polynom);

        pupilFunctionsLarge(:,:,trial) = pupilFunctionsLarge(:,:,trial) + ...
            getZernikeWeighted(size_zern,n,m,weight);

        pupilFunctionsSmall(:,:,trial) = pupilFunctionsSmall(:,:,trial) + ...
            getZernikeWeighted(size_zernSmall,n,m,weight);
    end

end
```

A.5 Zernike polynomial generation

This code is used to generate a single Zernike polynomial. It uses a third-party function called `zernfun` to obtain the polynomial. The `zernfun` code is available on the Matlab File Exchange website. This code is meant to be wrapped in another function that can return a weighted sum of a series of polynomials on the

unit disk.

```
function [ ZernikePolynomial ] = getZernikeWeighted( sz, n, m, weight )
    %GETZERNIKESWEIGHTED The n-m Zernike polynomial
    %   size - array size
    %   n - major order
    %   m - minor order - must be +/-(n-2)
    %   weight - cofficient of weight for the current polynomial

    step = 2/sz;
    xx = -1:step+eps:1;  % alternative to linspace
    [X,Y] = meshgrid(xx,xx);
    [theta,r] = cart2pol(X,Y);
    idx = r<=1;

    ZernikePolynomial = zeros(sz,sz);
    if weight ~= 0
        ZernikePolynomial(idx) = zernfun(n, m, r(idx), theta(idx));
        ZernikePolynomial = weight*pi*((ZernikePolynomial));
    end
end
```

A.6 OTF from autocorrelation of the pupil function

This code snippet illustrates the usage of the Zernike polynomial representation of wavefront aberrations for deriving the system OTF using the autocorrelation of the pupil function. Note that we use an efficient version of the autocorrelation function, which is nominally the convolution of the pupil function with itself. In this case, we used the point-wise multiplication of the discrete Fourier transform matrix of the pupil function.

```
%% Get the OTF with autocorrelation of the pupil function
% Here we derive the wavefront error from the zernike matrix. However, this
% time around we can use a smaller Zernike matrix, since we use the entire
% matrix for the OTF, and the OTF needs only to be the size of the beam.

% Autocorrelation returns a matrix with size 2n-1, so start with size n/2:
size_smallZern = size_beam/2;
% aberratedPupils = getZernikes(size_smallZern, modes_zern);

aberratedPupils = pupilFunctionsSmall;
[a,b,~]= size(aberratedPupils);
```

```
% Note the even length:
OTF = zeros(2*a, 2*b, num_trials);

% Use fft version, xcorr2 is VERY SLOW.
addpath 'xcorr2_fft/' -end

for i = 1:num_trials
    xcor = xcorr2_fft(aberratedPupils(:,:,i));
    otf = zeros(2*a,2*b);
    otf(1:end-1,1:end-1) = abs(xcor); % Incoherent otf: use magnitude (xcorr can be negative)
    otf(end,:) = ww;                  % Add the wgn vector to the last row
    otf(:,end) = ww';                 % and column
    OTF(:,:,i) = otf/max(otf(:));
end
```

Bibliography

[1] Muthuvel Arigovindan, John W Sedat, and David A Agard. Effect of depth dependent spherical aberrations in 3d structured illumination microscopy. *Optics express*, 20(6):6527–6541, 2012.

[2] Rodrigo Aviles-Espinosa, Jordi Andilla, Rafael Porcar-Guezenec, Omar E Olarte, Marta Nieto, Xavier Levecq, David Artigas, and Pablo Loza-Alvarez. Measurement and correction of in vivo sample aberrations employing a nonlinear guide-star in two-photon excited fluorescence microscopy. *Biomedical optics express*, 2(11):3135–3149, 2011.

[3] Oscar Azucena, Justin Crest, Jian Cao, William Sullivan, Peter Kner, Donald Gavel, Daren Dillon, Scot Olivier, and Joel Kubby. Wavefront aberration measurements and corrections through thick tissue using fluorescent microsphere reference beacons. *Optics express*, 18(16):17521–17532, 2010.

[4] Oscar Azucena, Justin Crest, Shaila Kotadia, William Sullivan, Xiaodong Tao, Marc Reinig, Donald Gavel, Scot Olivier, and Joel Kubby. Adaptive optics wide-field microscopy using direct wavefront sensing. *Optics letters*, 36(6):825–827, 2011.

[5] Eric Betzig. Single molecules, cells, and super-resolution optics.

[6] Eric Betzig, George H. Patterson, Rachid Sougrat, O. Wolf Lindwasser, Scott Olenych, Juan S. Bonifacino, Michael W. Davidson, Jennifer Lippincott-Schwartz, and Harald F. Hess. Imaging intracellular fluorescent proteins at nanometer resolution. *Science*, 313(5793):1642–1645, 2006.

[7] Martin Booth, Débora Andrade, Daniel Burke, Brian Patton, and Mantas Zurauskas. Aberrations and adaptive optics in super-resolution microscopy. *Microscopy*, page dfv033, 2015.

[8] Martin J Booth. Wave front sensor-less adaptive optics: a model-based approach using sphere packings. *Optics express*, 14(4):1339–1352, 2006.

[9] Martin J Booth, Mark AA Neil, Rimas Juškaitis, and Tony Wilson. Adaptive aberration correction in a confocal microscope. *Proceedings of the National Academy of Sciences*, 99(9):5788–5792, 2002.

[10] Max Born and Emil Wolf. *Principles of optics: electromagnetic theory of propagation, interference and diffraction of light*. CUP Archive, 2000.

[11] Diana C Chen, Steven M Jones, Dennis A Silva, and Scot S Olivier. High-resolution adaptive optics scanning laser ophthalmoscope with dual deformable mirrors. *JOSA A*, 24(5):1305–1312, 2007.

[12] Delphine Débarre, Edward J Botcherby, Martin J Booth, and Tony Wilson. Adaptive optics for structured illumination microscopy. *Optics express*, 16(13):9290–9305, 2008.

[13] Delphine Débarre, Edward J Botcherby, Tomoko Watanabe, Shankar Srinivas, Martin J Booth, and Tony Wilson. Image-based adaptive optics for two-photon microscopy. *Optics letters*, 34(16):2495–2497, 2009.

[14] Winfried Denk, James H. Strickler, Watt W. Webb, et al. Two-photon laser scanning fluorescence microscopy. *Science*, 248(4951):73–76, 1990.

[15] James R Fienup, Joseph C Marron, Timothy J Schulz, and John H Seldin. Hubble space telescope characterized by using phase-retrieval algorithms. *Applied optics*, 32(10):1747–1767, 1993.

[16] Peng Gao and G. Ulrich Nienhaus. Confocal laser scanning microscopy with spatiotemporal structured illumination. *Optics letters*, 41(6):1193–1196, 2016.

[17] Ralph W. Gerchberg. A practical algorithm for the determination of phase from image and diffraction plane pictures. *Optik*, 35:237, 1972.

[18] Joseph W Goodman. *Introduction to Fourier optics*. Roberts and Company Publishers, 2005.

[19] Min Gu. *Principles of three dimensional imaging in confocal microscopes*. World Scientific, 1996.

[20] Mats G.L. Gustafsson. Surpassing the lateral resolution limit by a factor of two using structured illumination microscopy. *Journal of microscopy*, 198(2):82–87, 2000.

[21] Mats GL Gustafsson. Nonlinear structured-illumination microscopy: wide-field fluorescence imaging with theoretically unlimited resolution. *Proceedings of the National Academy of Sciences of the United States of America*, 102(37):13081–13086, 2005.

[22] Mats GL Gustafsson, David A Agard, and John W Sedat. Doubling the lateral resolution of wide-field fluorescence microscopy using structured illumination. In *Three-Dimensional and Multidimensional Microscopy: Image Acquisition Processing VII*, volume 3919, pages 141–151. International Society for Optics and Photonics, 2000.

[23] Mats G.L. Gustafsson, Lin Shao, Peter M. Carlton, C.J. Rachel Wang, Inna N. Golubovskaya, W. Zacheus Cande, David A. Agard, and John W. Sedat. Three-dimensional resolution doubling in wide-field fluorescence microscopy by structured illumination. *Biophysical journal*, 94(12):4957–4970, 2008.

[24] John W Hardy. *Adaptive optics for astronomical telescopes*, volume 16. Oxford University Press on Demand, 1998.

[25] Stefan W. Hell and Jan Wichmann. Breaking the diffraction resolution limit by stimulated emission: stimulated-emission-depletion fluorescence microscopy. *Optics letters*, 19(11):780–782, 1994.

[26] Fritjof Helmchen and Winfried Denk. Deep tissue two-photon microscopy. *Nature methods*, 2(12):932, 2005.

[27] Nicholas G Horton, Ke Wang, Demirhan Kobat, Catharine G Clark, Frank W Wise, Chris B Schaffer, and Chris Xu. In vivo three-photon microscopy of subcortical structures within an intact mouse brain. *Nature photonics*, 7(3):205, 2013.

[28] Bo Huang, Hazen Babcock, and Xiaowei Zhuang. Breaking the diffraction barrier: super-resolution imaging of cells. *Cell*, 143(7):1047–1058, 2010.

[29] Francis A. Jenkins and Harvey E. White. *Fundamentals of optics*. Tata McGraw-Hill Education, 1957.

[30] Matthew Kissel, Marc Reinig, Oscar Azucena, Juan J Díaz León, and Joel Kubby. Development and testing of an ao-structured illumination microscope. In *MEMS Adaptive Optics VIII*, volume 8978, page 89780G. International Society for Optics and Photonics, 2014.

[31] Joel A. Kubby. *Adaptive Optics for Biological Imaging*. CRC press, 2013.

[32] Amit Lal, Chunyan Shan, and Peng Xi. Structured illumination microscopy image reconstruction algorithm. *IEEE Journal of Selected Topics in Quantum Electronics*, 22(4):1–14, 2016.

[33] Zhongchao Liao. A computer algorithm to implement linear structured illumination imaging. *Unpublished Master's thesis*, 2010.

[34] Jian Liu and Jiubin Tan. *Confocal Microscopy*. Morgan & Claypool Publishers, 2016.

[35] AW Lohmann and William T Rhodes. Two-pupil synthesis of optical transfer functions. *Applied optics*, 17(7):1141–1151, 1978.

[36] Stefano Marchesini. Invited article: A unified evaluation of iterative projection algorithms for phase retrieval. *Review of scientific instruments*, 78(1):011301, 2007.

[37] A Masson, M Pedrazzani, S Benrezzak, P Tchenio, T Preat, and D Nutarelli. Micromirror structured illumination microscope for high-speed in vivo drosophila brain imaging. *Optics express*, 22(2):1243–1256, 2014.

[38] Jerome Mertz. Optical sectioning microscopy with planar or structured illumination. *Nature methods*, 8(10):811, 2011.

[39] Jerome Mertz, Hari Paudel, and Thomas G Bifano. Field of view advantage of conjugate adaptive optics in microscopy applications. *Applied optics*, 54(11):3498–3506, 2015.

[40] Mark AA Neil, Rimas Juškaitis, and Tony Wilson. Method of obtaining optical sectioning by using structured light in a conventional microscope. *Optics letters*, 22(24):1905–1907, 1997.

[41] Mélanie Pedrazzani, Vincent Loriette, Paul Tchenio, Sakina Benrezzak, Daniele Nutarelli, and Alexandra Fragola. Sensorless adaptive optics implementation in widefield optical sectioning microscopy inside in vivo drosophila brain. *Journal of biomedical optics*, 21(3):036006, 2016.

[42] Ben C Platt and Roland Shack. History and principles of shack-hartmann wavefront sensing. *Journal of Refractive Surgery*, 17(5):S573–S577, 2001.

[43] Jason Porter, Hope Queener, Julianna Lin, Karen Thorn, and Abdul AS Awwal. *Adaptive optics for vision science: principles, practices, design and applications*, volume 171. John Wiley & Sons, 2006.

[44] Milind Rajadhyaksha, Melanie Grossman, Dina Esterowitz, Robert H Webb, and R Rox Anderson. In vivo confocal scanning laser microscopy of human skin: melanin provides strong contrast. *Journal of Investigative Dermatology*, 104(6):946–952, 1995.

[45] Lord Rayleigh. Xxxi. investigations in optics, with special reference to the spectroscope. *The London, Edinburgh, and Dublin Philosophical Magazine and Journal of Science*, 8(49):261–274, 1879.

[46] Marc R Reinig, Samuel W Novak, Xiaodong Tao, Laurent A Bentolila, Dustin G Roberts, Allan MacKenzie-Graham, Sirie E Godshalk, Mary A Raven, David W Knowles, and Joel Kubby. Enhancing image quality in cleared tissue with adaptive optics. *Journal of biomedical optics*, 21(12):121508, 2016.

[47] Michael J. Rust, Mark Bates, and Xiaowei Zhuang. Sub-diffraction-limit imaging by stochastic optical reconstruction microscopy (storm). *Nature methods*, 3(10):793–796, 2006.

[48] Lothar Schermelleh, Rainer Heintzmann, and Heinrich Leonhardt. A guide to super-resolution fluorescence microscopy. *The Journal of cell biology*, 190(2):165–175, 2010.

[49] C.J.R. Sheppard and Min Gu. Image formation in two-photon fluorescence microscopy. *Optik*, 86(3):104–106, 1990.

[50] Sapna A. Shroff, James R. Fienup, and David R. Williams. Otf compensation in structured illumination superresolution images. In *Optical Engineering+ Applications*, pages 709402–709402. International Society for Optics and Photonics, 2008.

[51] Qiyuan Song, Keisuke Isobe, Kenichi Hirosawa, Katsumi Midorikawa, and Fumihiko Kannari. 2d simultaneous spatial and temporal focusing multiphoton microscopy for fast volume imaging with improved sectioning ability. In *Multiphoton Microscopy in the Biomedical Sciences XV*, volume 9329, page 93292N. International Society for Optics and Photonics, 2015.

[52] Ernst HK Stelzer. Light-sheet fluorescence microscopy for quantitative biology. *Nat. Methods*, 12(1):23–26, 2015.

[53] Xiaodong Tao, Dare Bodington, Marc Reinig, and Joel Kubby. High-speed scanning interferometric focusing by fast measurement of binary transmission matrix for channel demixing. *Optics express*, 23(11):14168–14187, 2015.

[54] Xiaodong Tao, Justin Crest, Shaila Kotadia, Oscar Azucena, Diana C Chen, William Sullivan, and Joel Kubby. Live imaging using adaptive optics with fluorescent protein guide-stars. *Optics express*, 20(14):15969–15982, 2012.

[55] Xiaodong Tao, Bautista Fernandez, Oscar Azucena, Min Fu, Denise Garcia, Yi Zuo, Diana C. Chen, and Joel Kubby. Adaptive optics confocal microscopy using direct wavefront sensing. *Optics letters*, 36(7):1062–1064, 2011.

[56] Xiaodong Tao, Andrew Norton, Matthew Kissel, Oscar Azucena, and Joel Kubby. Adaptive optical two-photon microscopy using autofluorescent guide stars. *Optics letters*, 38(23):5075–5078, 2013.

[57] Benjamin Thomas, Adrian Wolstenholme, Snehal N Chaudhari, Edward T Kipreos, and Peter Kner. Enhanced resolution through thick tissue with structured illumination and adaptive optics. *Journal of biomedical optics*, 20(2):026006–026006, 2015.

[58] Vikas Trivedi, Thai V Truong, Le A Trinh, Daniel B Holland, Michael Liebling, and Scott E Fraser. Dynamic structure and protein expression of the live embryonic heart captured by 2-photon light sheet microscopy and retrospective registration. *Biomedical optics express*, 6(6):2056–2066, 2015.

[59] Pierre Vermeulen, Eleonora Muro, Thomas Pons, Vincent Loriette, and Alexandra Fragola. Adaptive optics for fluorescence wide-field microscopy using spectrally independent guide star and markers. *Journal of Biomedical Optics*, 16(7):076019, 2011.

[60] Peter W. Winter, Andrew G. York, Damian Dalle Nogare, Maria Ingaramo, Ryan Christensen, Ajay Chitnis, George H. Patterson, and Hari Shroff. Two-photon instant structured illumination microscopy improves the depth penetration of super-resolution imaging in thick scattering samples. *Optica*, 1(3):181–191, 2014.

[61] Tsai-wei Wu and Meng Cui. Numerical study of multi-conjugate large area wavefront correction for deep tissue microscopy. *Optics express*, 23(6):7463–7470, 2015.

[62] Chia-Hua Yeh and Szu-Yu Chen. Resolution enhancement of two-photon microscopy via intensity-modulated laser scanning structured illumination. *Applied optics*, 54(9):2309–2317, 2015.

[63] Andrew G. York, Panagiotis Chandris, Damian Dalle Nogare, Jeffrey Head, Peter Wawrzusin, Robert S. Fischer, Ajay Chitnis, and Hari Shroff. Instant super-resolution imaging in live cells and embryos via analog image processing. *Nature methods*, 10(11):1122–1126, 2013.

[64] Andrew G. York, Sapun H. Parekh, Damian Dalle Nogare, Robert S. Fischer, Kelsey Temprine, Marina Mione, Ajay B. Chitnis, Christian A. Combs, and Hari Shroff. Resolution doubling in live, multicellular organisms via multifocal structured illumination microscopy. *Nature methods*, 9(7):749–754, 2012.